

Experimental measurement of dislocation density in metallic materials: A quantitative comparison between measurements techniques (XRD, R-ECI, HR-EBSD, TEM)

J. Gallet^a, M. Perez^a, R. Guillou^b, C. Ernould^{c,d}, C. Le Bourlot^a, C. Langlois^a, B. Beausir^{c,d}, E. Bouzy^{c,d}, T. Chaise^e, S. Cazottes^{a,*}

^a Université de Lyon, INSA Lyon, UCBL, MATEIS, UMR CNRS 5510, France

^b Université Paris-Saclay, CEA, Service de Recherches Métallurgiques Appliquées, 91191, Gif sur Yvette, France

^c Université de Lorraine, CNRS, LEM3, F-57000 Metz, France

^d Laboratory of Excellence on Design of Alloy Metals for low-mAss Structures (DAMAS), University of Lorraine, 57073 Metz, France.

^e Univ Lyon, INSA Lyon, CNRS, LaMCoS, UMR 5259, 69621 Villeurbanne, France

ARTICLE INFO

Keywords:

Dislocation density
ECI
TEM
XRD
HR EBSD
EBSD

ABSTRACT

The dislocation densities were measured on the same samples using transmission electron microscopy (TEM), scanning electron microscopy (electron channeling contrast imaging (ECI) and high-angular-resolution-electron backscattered diffraction (HR-EBSD)), and X-ray diffraction (XRD). Notably, these different methods do not observe the same types of dislocations, i.e., statistically stored dislocations (SSDs) and/or geometrically necessary dislocations (GNDs). ECI and TEM imaging are direct-measurement techniques, whereas HR-EBSD and XRD are indirect methods. Therefore, a quantitative comparison of the measurements obtained using these four techniques on undeformed and deformed duplex steels is proposed. For low deformation, where the dislocation density is quite small ($1 - 5 \times 10^{13} \text{ m}^{-2}$), imaging methods are rather performant, whereas XRD measurements suffer from high uncertainty levels. HR-EBSD measurements show results that are in good agreement with the other methods for these deformation levels. For higher deformation levels (with dislocation densities above $1 - 3 \times 10^{14} \text{ m}^{-2}$), imaging methods are no longer relevant because of the increasing uncertainty arising from local contrast variation and overlapping of dislocations. The different results obtained highlight the necessity of taking a step back on each method used. Correctly defining what is to be measured (SSDs or GNDs), in which condition (solid material or thin plate) as well as the parameters (pixel size, area, etc.) and their bias is essential, especially if the objective is to use the measurement in a micromechanical model.

1. Introduction

The plastic deformation of materials comes from the ability of crystal lattices to shear through the movements of dislocations. The interactions of the different mechanisms of deformation are complex and depend on each other. Their understanding is necessary, and a precise observation of these phenomena must be performed in order to take them into account when building theoretical models at the microstructural scale [1–4]. For example, Mecking et al. [5,6] and Estrin et al. [7,8] proposed yield strength and hardening models using the dislocation density ρ as a key parameter. Blaizot et al. [1,9] confirmed experimentally that Mecking's theory could be applied to describe the impact of the

dislocation density on the yield strength in the case of nickel-based alloys, whereas Diano et al. [10] experimentally showed that the tensile properties are mainly controlled by the grain size and dislocation density.

Although different methods have been developed, experimental measurement of the dislocation density in metallic alloys remains a challenging task. Indeed, for each measurement method, experimental artifacts induce non-negligible bias that must be considered. Beyond the definition of dislocations from the crystallographic point of view, their modelling implies concepts or units that differ from the metallurgical ones at some point (e.g., expressing densities in m^{-1} rather than m^{-2}).

Dislocations in polycrystalline materials can usually be found either

* Corresponding author.

E-mail address: sophie.cazottes@insa-lyon.fr (S. Cazottes).

<https://doi.org/10.1016/j.matchar.2023.112842>

Received 18 October 2022; Received in revised form 1 March 2023; Accepted 21 March 2023

Available online 23 March 2023

1044-5803/© 2023 Elsevier Inc. All rights reserved.

isolated, randomly distributed inside the cells or grains, or localized close to grain boundaries to accommodate possible strain incompatibilities between the different grains. Other dislocations are found to be organized into patterns, in the form of dislocation cells or walls.

Therefore the total dislocation density ρ_{tot} is often decomposed as [11,12]:

$$\rho_{\text{tot}} = \rho_W + \rho_c + \rho_{\text{GB}} \quad (1)$$

where ρ_W is the density of dislocations constituting the cell walls, ρ_c is the dislocation density randomly distributed within the cells/grains, and ρ_{GB} is the dislocation density present at grain boundaries.

Another description of dislocations is often given, namely geometrically necessary dislocations (GNDs) and statistically stored dislocations (SSDs), as presented by Nye [13], Cottrell [14], and Ashby [15]. GNDs play an important role in the strengthening effects of alloys [16,17]. They are related to the deformation gradients arising from the geometric constraints of the crystal lattice. These “same-sign” dislocations induce lattice curvature, or local disorientation, and represent dislocations more often located at grain boundaries or cells walls such that the total amount of GNDs can also be expressed as $\rho_{\text{GND}} = \rho_W + \rho_{\text{GB}}$. On the other end, SSDs are stored due to an accumulation process — they trap each other randomly and do not produce significant disorientation [18]. These dislocations represent the random distribution of dislocations, described by ρ_c . Hence, the total dislocation density is often rewritten simply as

$$\rho_{\text{tot}} = \rho_{\text{GND}} + \rho_{\text{SSD}}$$

The experimental determination of the dislocation density can be achieved using different methods, including imaging methods such as transmission electron microscopy (TEM), electron channeling contrast imaging in the scanning electron microscope (ECCI), or diffraction-based methods such as electron backscattered diffraction (EBSD), high-resolution-EBSD (HR-EBSD), or X-ray diffraction (XRD).

It should be noted, however, that each method does not characterize the same dislocation populations.

Dislocation imaging methods such as TEM or ECCI theoretically allow the observation of all the dislocations in the analyzed volume. The dislocation density is usually obtained by counting the visible dislocations in the analyzed areas and applying a derivate of the general formula $\rho_{\text{tot}} = L/V$ [19], where V is the analyzed volume and L is the total dislocation length of visible dislocations. The main experimental bias leading to measurement uncertainties involves the determination of the probed thickness and thus the volume as well as the impossibility of observing all the dislocations at once. Indeed, due to the invisibility rule [20], only part of the dislocations are visible. Moreover, for dislocations located at grain boundaries and organized in walls, counting individual dislocations becomes rather difficult and inaccurate when they overlap/start overlapping. Dislocation counting on TEM or ECCI images in such a case is therefore a tedious task. To overcome this issue, a new methodology was recently developed based on ECCI imaging. A series of ECCI images are first recorded while rotating the sample and then automatically analyzed using a clustering-based algorithm, from which the dislocation density is derived [21,22].

EBSD is mostly used to characterize microstructures using orientation maps. Indeed, the GND density is then computed from the local crystal curvature (through the local disorientation θ) and the map step size [7,13,23–25]. Although common, this approach is questionable. The uncertainty of the crystallographic orientations limits the sensitivity on GND densities, with the resulting disorientation axis being significantly imprecise for low disorientation angles [26]. The weighed Burgers vector method proposes to consider a kind of Burgers circuit in order to reduce the imprecision at low disorientation angles [27]; however, only three components of the curvature tensor are considered and the contribution of elastic strain is also neglected. The latter is

nevertheless a reasonable assumption in plastically deformed metals [28,29] but not in slightly disoriented materials such as in GaN single crystals [29].

As a solution, the high (angular)-resolution EBSD (HR-EBSD) technique was developed under the impetus of Wilkinson et al. [30] and recently experienced a revival with the emergence of global image registration approaches [31–33], such as the method used in [34,35]. All these methods apply digital image correlation techniques to a pair of Kikuchi patterns in order to measure their relative displacement field with subpixel accuracy. Coupled with the precise knowledge of the projection geometry, the relative lattice rotation and elastic strain can be captured with a typical accuracy of 10^{-4} ($> 0.006^\circ$) under good experimental conditions. The Nye's tensor can then be calculated, including the contribution of the elastic strains [36]. The complete determination of this tensor, however, remains limited by the two-dimensional nature of EBSD measurements, hence the growing interest in 3D HR-EBSD studies such as those in [37]. The higher accuracy of HR-EBSD techniques as compared to an indexing-based GND derivation is associated with practical considerations limiting its wider use: the use of a high-resolution camera with longer exposure time and large data collection (15–20 GB for the maps used in this article), with each diffraction pattern being stored for the subsequent numerically intensive data post-processing. Therefore, identifying the cases of applications where the method brings a real improvement compared to indexing, in particular for deformed polycrystals, is crucial [34,38–40].

XRD is a more global measurement technique that is often performed on a much larger volume, which, in the present case, will contain many grains of both phases with different orientations, and this different deformation behavior. The calculation of the dislocation density by XRD is based on the broadening of the diffraction peak, which appears to be more sensitive to the SSD dislocation type [12]. Indeed, the calculation assumes the presence of ‘crystallite domains’ that would correspond to the cell/structure. Therefore, dislocations present at cells or grain boundaries would not be taken into account. This limitation was experimentally confirmed by a direct comparison of TEM and XRD measurements made on copper single crystals by Ungar et al. [41].

Nowadays, in order to get a correct measurement of the dislocation population, the complementary use of diffraction and imaging techniques is often performed [42,43]. However, the measurements do often provide different results, and it is yet unclear how these results can be used as input in micromechanical models.

This study is dedicated to the determination of the best methodology to apply for the characterization of dislocation densities that can be used as input in micro-mechanical modellings. The aim of the current paper is (i) to present some quantitative measurements of dislocation densities performed on the same duplex steel samples using four different characterization techniques and for three different strain levels, (ii) to discuss the measurement uncertainties of all the applied techniques, and (iii) to discuss the link between the obtained results and the different types of dislocations observed for each method.

2. Materials and methods

2.1. Materials

In order to better discuss the potential of each characterization method (local and global), a two-phase alloy, whose microstructure is therefore heterogeneous, was chosen as a study material. Observations were made on a commercial hot-rolled Outokumpu 2101 lean duplex stainless steel. This material was chosen as different dislocation densities are expected in the two phases after deformation, and several mechanical models exist to describe the plastic deformation of both phases [44–46]. The selection of this material was motivated by the presence of two phases, austenite and ferrite, in which the dislocations adopt very distinct arrangements. Indeed, the dislocations appear straight with a high contrast and variable thickness in the austenitic phase, which

makes them easy to image. In the ferritic phase, in contrast, the dislocations appear tortuous with a lower contrast, which makes them more difficult to image. It is therefore interesting to study the performance of measurement methods based on dislocation imaging (ECCI/TEM) for this material and, more particularly, the R-ECCI method.

The evolution of the dislocation density was characterized in both the ferritic and austenitic phases. Microtensile samples (total length 112.5 mm, width 12.5 mm, and thickness of 1.5 mm) were deformed under an optical microscope using a Deben 2000E tensile stage. Using standard digital image correlation (DIC), the deformation was determined on all points of the surface. One sample was deformed to 5% and the other one to 10%. In the present study, the austenite grain size will be affected by the appearance of martensite in austenite during deformation.

For the ECCI and HR-EBSD measurements, the samples were mechanically ground, and the final polishing was performed using a 1- μm diamond solution. To avoid any strain hardening of the surface, a final electropolishing step was performed using A2 electrolyte (from Struers APS, Denmark) at 20 V for 60 s with a Lectropol 5 device (Struers APS, Denmark).

To allow for the TEM observations, the duplex samples were mechanically ground to obtain a thin sample of 50- μm thickness. Small discs of 3-mm diameter were subsequently extracted by punching and later electropolished using A2 electrolyte (from Struers APS, Denmark) with a Tenupol-5 device (Struers APS, Denmark). A final ion-polishing step was performed using PIPS-II to increase the observable area with an acceleration voltage of 1.5 keV and angles of $\pm 4^\circ$ for the ion beams for 2 h.

For the XRD measurements, the samples were mechanically ground down to a 1200P using SiC paper.

3. Methods

3.1. Transmission Electron Microscopy

TEM micrographs were acquired with a TEM JEOL 2100 LaB6 operating at 200 kV. For the dislocation density measurements, the intercept method was used [47]. This method consists of drawing lines of total length l on the image (arbitrary lines or a regular grid) and counting the number of intersections n with dislocations. The dislocation density ρ is then calculated using the formula $\rho = \frac{2n}{l}$, where t is the analyzed thickness. The determination of t was achieved by measuring the number of thickness fringes [48]. For a grain in a given two-beam orientation, the probed depth z is proportional to the number of bands N observed, and the extinction distance ξ_g related to the diffraction vector used: $z = (N - \frac{1}{2}) \xi_g$.

The observation of dislocations in TEM is possible in weak-beam dark-field (WBDF) mode [49] or in bright-field (BF) mode. In both cases, the crystal must be oriented in a two-beam (TB) [50] condition (only one diffracting vector \vec{g}_{hkl}). Under these conditions, only screw dislocations with a Burgers vector \vec{b} respecting the relation $\vec{g}_{hkl} \cdot \vec{b} \neq 0$ are visible, whereas the condition for edge dislocations is $\vec{g}_{hkl} \cdot \vec{b} \times \vec{u} \neq 0$. As a result, for each orientation condition, different dislocations might be invisible, and the density is then always underestimated when determined from only one orientation condition. Therefore, for each strain rate and for each phase, two to three grains of each phase were oriented under several TB conditions.

3.2. R-electron channeling contrast imaging

SEM-ECCI observations were performed on a Zeiss Supra 55VP SEM with an accelerating voltage of 20 keV, a 120- μm diaphragm, and a working distance close to 7 mm. The SEM images were recorded with a pixel size of 4.5 nm and a size of 1024 \times 768 pixels.

A series of BSE rotation images were acquired following the procedure presented in [51,52]. For each pixel in the imaging series, the intensity variation as a function of the rotation angle can be plotted and is called the intensity profile. The main intensity profile of a given grain is a signature of its crystallographic orientation [53]. For dislocation pixels, the intensity profile close to the rotation angle corresponding to a visibility condition will differ slightly from that of the corresponding grains. A clustering algorithm, presented in [52], was developed to calculate the intensity difference between every pixel and the mean intensity profile of each grain, such that the nature of each pixel could be identified: dislocation, matrix, or noise. The dislocation density ρ_{clus} of a given area is then calculated using the general formula $\rho_{clus} = \frac{L}{V}$, where L is the dislocation length contained in the volume V . After data treatment, the total number of dislocation pixels N^{dislo} is determined. The total length of the dislocations is then calculated using

$$L^{dislo} = \frac{N^{dislo} \times P_S}{E}, \quad (2)$$

where E is the mean thickness of the dislocations (in pixels) and P_S is the pixel size in nm. E is defined as

$$E = E^{app} / P_S, \quad (3)$$

where E^{app} is the apparent dislocation width in nm, which is manually determined from the imaging series. The dislocation density ρ is obtained from the following relation:

$$\rho = \frac{N^{dislo} \times P_S}{S \times t \times E} = \frac{N^{dislo} \times P_S \times 2}{N^{tot} \times P_S \times 2 \times t \times E^{app}} = \frac{N^{dislo}}{N^{tot} \times t \times E^{app}}, \quad (4)$$

where t is the analyzed sample thickness (in nm) and S is the analyzed surface in nm^2 . N^{tot} is the total number of pixels in each image series. Therefore, the dislocation density ρ only depends on E^{app} measured manually from the image and on t , the analyzed thickness. The value selected for the interaction depth is $3\xi_g$ (approximately 93 nm for \vec{g}_{200} in ferrite and 114 nm for \vec{g}_{220} in austenite), in agreement with the predictions made by Zaefferer from ECCI simulations [54].

3.3. EBSD and high angular resolution EBSD

EBSD was conducted using the same microscope as that used for the R-ECCI acquisitions. Electron backscatter diffraction patterns (EBSPs) were obtained using an EBSD Symmetry camera (Oxford), an acceleration voltage of 15 kV, an exposure time of 32 ms, an aperture of 60 μm , and a pixel size of 50 nm. The EBSP images were averaged by 3 to enhance their signal-to-noise ratio in view of the subsequent HR-EBSD analysis.

The latter is based on a global image registration approach implemented in ATEX software (developed at the University of Lorraine) [55]. EBSPs are considered as a whole, through a unique and large region of interest, whose relative deformations are modelled by linear homography [34]. Often used in computer vision to describe projections, the latter is measured by an iterative inverse-compositional Gauss–Newton algorithm, modified to integrate a correction of optical distortions caused by camera lenses [56]. The reader is also referred to chapters 3 to 5 in [35] for further details.

The Nye's dislocation tensor is computed according to the Nye–Kröner theory [13,36]:

$$\alpha = \text{curl } \epsilon + \text{tr}(\kappa_e) \cdot I - \kappa_e^T, \quad (5)$$

where ϵ is the elastic strain tensor and κ_e is the lattice curvature. These curvatures can be approximated using a finite difference scheme:

$$\kappa_{ij} \cong \Delta w_i / \Delta x_j, \quad (6)$$

where Δw_i is the difference of rotation w_i (with respect to the axes of the

basis) between two neighboring points separated spatially by Δx_j in the j -th direction. Thus, the GND densities obtained by EBSD or HR-EBSD depend on the step size [57,58], which will be further discussed later in this study.

Regarding the HR-EBSD technique, relative lattice rotations w_i between the reference and the target as well as the elastic strains are directly obtained. For standard EBSD, the contribution of elastic strains is unknown and simply omitted while the lattice rotations w_i are derived from the Euler angles [23]. Given two points “A” and “B” of the material, their respective orientation matrices \mathbf{g}_A and \mathbf{g}_B are computed, and the disorientation angle $\Delta\theta$ is then deduced:

$$\Delta\theta = \min_k \left[\arccos \left(\frac{\text{tr}(\Delta \mathbf{g}^k) - 1}{2} \right) \right], \quad (7)$$

where $\Delta \mathbf{g}^k$ is the “disorientation” matrix for the k -th symmetry of the crystal. This disorientation is decomposed into three rotations w_i with respect to the axes X_i of the sample frame:

$$w_i = -e_{ijk} \cdot \Delta g_{ij} \cdot \frac{\Delta\theta}{2 \cdot \sin(\Delta\theta)}, \quad (8)$$

where e_{ijk} is the permutation symbol of Levi-Civita. The lattice rotations are evaluated considering the same reference point as in the HR-EBSD analysis. On the one hand, the location of this reference is not important from a strictly mathematical point of view, with the calculation of the Nye tensor implying spatial derivatives. On the other hand, the grain internal disorientation angle is generally smaller between neighboring pixels. As mentioned in the introduction, this factor is detrimental to the accuracy on the disorientation axis [26] and the rotations w_i accordingly.

For both EBSD and HR-EBSD, only a partial computation of the Nye’s dislocation tensor is possible. Indeed, the latter implies spatial derivatives along the surface normal direction (\vec{X}_3), which are unknown due to the two-dimensional nature of EBSD measurements:

$$\alpha = \begin{bmatrix} \frac{\partial \varepsilon_{12}}{\partial x_3} - \frac{\partial \varepsilon_{13}}{\partial x_2} & \frac{\partial \varepsilon_{13}}{\partial x_1} - \frac{\partial \varepsilon_{11}}{\partial x_3} & \frac{\partial \varepsilon_{11}}{\partial x_2} - \frac{\partial \varepsilon_{12}}{\partial x_1} \\ \frac{\partial \varepsilon_{22}}{\partial x_3} - \frac{\partial \varepsilon_{23}}{\partial x_2} & \frac{\partial \varepsilon_{23}}{\partial x_1} - \frac{\partial \varepsilon_{21}}{\partial x_3} & \frac{\partial \varepsilon_{21}}{\partial x_2} - \frac{\partial \varepsilon_{22}}{\partial x_1} \\ \frac{\partial \varepsilon_{32}}{\partial x_3} - \frac{\partial \varepsilon_{33}}{\partial x_2} & \frac{\partial \varepsilon_{33}}{\partial x_1} - \frac{\partial \varepsilon_{31}}{\partial x_3} & \frac{\partial \varepsilon_{31}}{\partial x_2} - \frac{\partial \varepsilon_{32}}{\partial x_1} \end{bmatrix} + \begin{bmatrix} \frac{\partial w_{12}}{\partial x_3} + \frac{\partial w_{31}}{\partial x_2} & \frac{\partial w_{13}}{\partial x_1} & \frac{\partial w_{21}}{\partial x_1} \\ \frac{\partial w_{32}}{\partial x_2} & \frac{\partial w_{23}}{\partial x_1} + \frac{\partial w_{12}}{\partial x_3} & \frac{\partial w_{21}}{\partial x_2} \\ \frac{\partial w_{32}}{\partial x_3} & \frac{\partial w_{13}}{\partial x_3} & \frac{\partial w_{31}}{\partial x_2} + \frac{\partial w_{23}}{\partial x_1} \end{bmatrix}, \quad (9)$$

where

$$w_{ij} = -e_{ijk} w_k, \quad (10)$$

i.e.,

$$\begin{cases} w_1 = w_{32} = -w_{23} \\ w_2 = w_{13} = -w_{31} \\ w_3 = w_{21} = -w_{12} \end{cases} \quad (11)$$

As a consequence, only the α_{13} , α_{23} , and α_{33} components are fully assessable [23–25]. The α_{12} and α_{21} components are determined by neglecting the contribution of elastic strains, which is partly unknown. Finally, the components α_{31} and α_{32} are not computable, with neither the contribution of lattice curvatures nor that of elastic strains being fully assessable.

In this study, both EBSD and HR-EBSD results are discussed from the norm of the estimated Nye’s tensor. Its α_{ij} components having units of inverse length are divided by the norm b of the Burgers vector to express

Table 1

: Summary of diffraction vectors used to characterize the three austenite grains and three ferrite grains, for different strain rates.

	Austenite			Ferrite		
	Sample 1 0%	Sample 2 5%	Sample 3 10%	Sample 1 0%	Sample 2 5%	Sample 3 10%
Diffracting vectors	(111) (220) (311)	(111) (110)	(111)	(101) (110) (112)	(011) (100) (211)	(110) (211)
Diffracting vectors	(111)	(110) (111)	(110)	(110) (020)	(110)	(110)
Diffracting vectors	(202) (111)	(111) (110) (311)	(111)	(011)		

a GND density in m^{-2} :

$$\rho_{\text{GND}} = \frac{1}{b} \sqrt{\alpha_{ij} \cdot \alpha_{ij}}. \quad (12)$$

3.4. X-ray diffraction

The XRD experiments were conducted using a Bruker D8 Advance diffractometer equipped with Mo-K α radiation ($\lambda_{\text{K}\alpha 1} = 0.7093 \text{ \AA}$), a Zr filter to absorb the K_{β} radiation from molybdenum, a 1-mm collimator, and a Lynxeye linear detector. The goniometer was operated in a θ/θ configuration: the X-ray tube and the detector move symmetrically while the sample remains horizontal in a fixed central location. Estimation of the crystallite size, D , as well as the microstrain, RMS (root mean square), was obtained by XRD line broadening using the Popa model integrated in the software MAUD.

XRD diagrams were fitted with a pseudo-Voigt function in the software MAUD [59]. Instrumental parameters for the fit (Caglioti parameters, Lorentzian/Gaussian ratio) were determined on a standard NIST

powder of hexaboride of lanthanum (LaB₆). The formula proposed by Murugesan et al. [60] for the dislocation density calculation was used.

The dislocation density ρ can be decomposed into two contributions:

$$\rho = (\rho_D \times \rho_S)^{1/2}, \quad (13)$$

where ρ_D is the domain contribution $\rho_D = \frac{3}{b^2}$ and ρ_S is the deformation contribution $\rho_S = \frac{k \langle \varepsilon_L^2 \rangle}{b^2} = \frac{k \langle \varepsilon_L^2 \rangle \sqrt{2}}{a^2}$ with the material constant k , crystallite size D , RMS micro strain $\langle \varepsilon_L^2 \rangle$, and Burgers vector b (here, $b = \frac{a}{\sqrt{2}}$). All the uncertainties were calculated from the formulas given by Murugesan et al. [61].

4. Results

4.1. Transmission electron microscopy

For each strain rate and for each phase, two to three grains of each phase were orientated in several TB conditions. All the g_{hkl} diffracting

vectors used for the analysis are listed in Table 1. The acquisition of dislocation images on the 10% deformed sample was difficult because of the strong disorientation present in the grains ($\sim 5^\circ$ – 6° for the most disoriented areas), and fewer diffraction conditions were observed for that sample. To limit the underestimation, the dislocation density selected for each grain was recorded as the maximum one measured in the different orientation conditions.

The analyzed area slightly varied for the different samples. For the 5% and 10% deformed grains, the average image area was 0.5 and 0.3 μm^2 , respectively, whereas it was 3.5 μm^2 for the undeformed sample. Indeed, for high deformation levels, the disorientation within each grain increases. Therefore, contrast conditions vary rapidly, and the observable areas on each image are reduced. Moreover, with increasing dislocation densities, dislocation overlapping increases. It is then necessary to enhance the magnification in order to achieve sufficient resolution to distinguish the dislocations from each other.

Figure 1 presents typical TB TEM micrographs obtained in austenite and ferrite for undeformed samples and samples deformed at 5% and 10%. The dislocations appear in black on a white background.

In the undeformed state, only a few dislocations are observable in the austenite in Fig. 1(a). The density seems higher in ferrite (Fig. 1(b)), where dislocations appear as points or lines, which reveals that their orientation in the grain is random. After 5% deformation, the number of visible dislocations greatly increased. In Fig. 1(d), the dislocations in the 5% deformed ferrite have clustered and become more tortuous. The overlapping of dislocations is important, as in the deformed austenite (Fig. 1(c)). For the 10% deformed sample (Fig. 1 (e) and (f)), it was quite difficult to image dislocations over large surfaces because the important disorientation locally modifies the contrast conditions. However, there is not much difference in the resulting micrographs compared with the 5% deformed sample. It is necessary to recall that the local thickness of the diverse thin foil is quite different. For example, for the deformed ferrite at 5%, it was measured to be 220 ± 37 nm, whereas it was 146 ± 37 nm for the 10% deformed sample (Fig. 1 (d) and (f)). Thus, a direct-

Table 2

: Mean value of the dislocation density (m^{-2}) obtained on ferrite and austenite grains for different strain rates measured from TEM imaging.

	0%	5%	10%
Austenite	$(1.1 \pm 0.1) \times 10^{13}$	$(6.7 \pm 1.0) \times 10^{13}$	$(1.4 \pm 0.3) \times 10^{14}$
Ferrite	$(1.2 \pm 0.1) \times 10^{13}$	$(5.7 \pm 0.8) \times 10^{13}$	$(1.2 \pm 0.2) \times 10^{14}$

eye comparison of the images can be misleading.

The dislocation densities were determined using the intercept method. The maximum values for each deformation level and phase are presented in Table 2.

The dislocation density was measured to be similar in both phases. As expected, the dislocation density increased with deformation, with a slightly more rapid increase in austenite compared to ferrite, as austenite deforms before ferrite [62]. After 10% deformation, the dislocation densities measured in ferrite and in austenite were approximately 10 times higher than before deformation. However, in the 10% deformed sample, it was very difficult to observe the dislocations on a large surface in a single image because of the deformation but also because of the thin foil, which was slightly twisted. This issue added to the difficulty of observing the dislocations but also to the measurement, especially at the top of the image of the 10% deformed ferrite (Fig. 1(f)). For this reason, the measurement uncertainty increases for the latter values, as it becomes problematic to distinguish dislocations from each other because of the overlapping of dislocations and the rapidly changing observation conditions as well as the uncertainty of the volume.

4.2. R-ECCI and clustering

The ECCI method allows the observation of dislocations in white on a black background. In the received state, Fig. 2(a and b), the dislocations

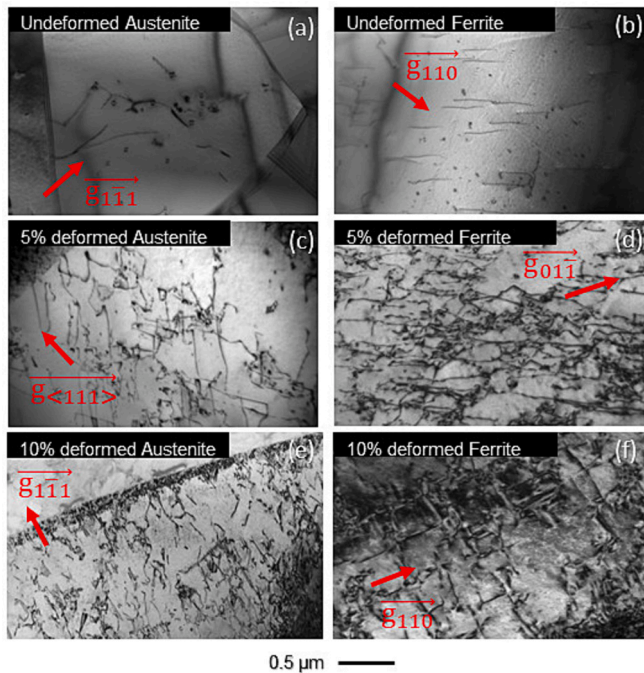


Fig. 1. TEM image acquired on different grains. For each image, the dislocation lines are visible in black on a white background. (a) Undeformed austenite grain. (b) Austenite grain in sample deformed at 5%. (c) Austenite grain in sample deformed at 10%. (d) Undeformed ferrite grain. (e) Ferrite grain in sample deformed at 5%. (f) Ferrite grain in sample deformed at 10%.

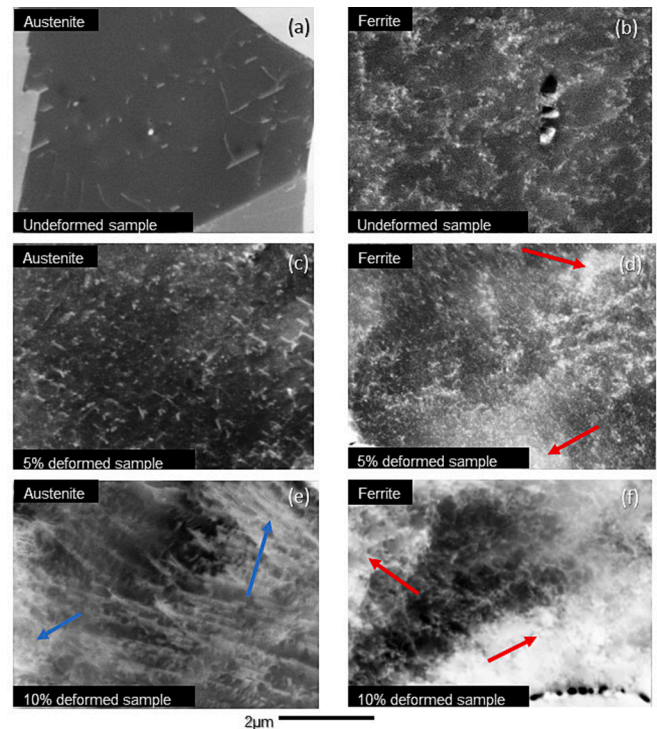


Fig. 2. BSE image acquired with an accelerating voltage of 20 keV, aperture of 120 μm , and pixel size of 4.5 nm. (a), (c), and (e) show three austenite grains present in an undeformed, 5% deformed, and 10% deformed sample, respectively. Similarly, images (b), (d), and (f) show three ferrite grains present in an undeformed, 5% deformed, and 10% deformed sample, respectively.

appear as straight lines or as dots, indicating that they are rather parallel or perpendicular to the surface, respectively. Moreover, at first sight, there would be more dislocations in the ferrite in the ECCI images (Fig. 2 (b)) than in the TEM images (Fig. 1 (b)), which could be due to the smaller thickness observed in the TEM images. In austenite, after deformation, the dislocations appeared as straight lines and were mainly aligned along the $\{111\}$ planes, Fig. 2(c) and (e). The high concentration of dislocations in the 10% deformed austenite (Fig. 2(e), blue arrow) resulted in a large variation in contrast, especially at the grain boundaries, making it difficult to detect dislocations using the clustering algorithm. In contrast, the dislocations in the ferrite in Fig. 2 (b, d and f) are more tortuous and appear to have random directions, including in the deformed cases, Fig. 2 (d and f). Moreover, the contrast variations are already visible after 5% in the deformed ferrite, Fig. 2 (d), and become even more significant after 10% deformation (as indicated by the red arrows).

After analysis, the detected dislocations were represented as green pixels on a dark matrix, as shown in Fig. 3 (b), (d), and (f) for the undeformed, 5% deformed, and 10% deformed sample, respectively. The dislocation density calculated by the clustering algorithm was $(1.5 \pm$

$0.1) \times 10^{13} \text{ m}^{-2}$ for undeformed austenite (Fig. 3 (a) and (b)), for which almost all dislocations were detected. This first case illustrates the effectiveness of the algorithm when the dislocations are distinct with a good contrast with the grain. For the ferrite after 5% deformation, the BSE image in Fig. 3 (c) shows more clustered dislocations that are more difficult to distinguish (blue circle). In that area, some dislocations are not indexed by the algorithm, Fig. 3 (d), and a local underestimation of the density is expected. Moreover, in certain other areas, the large amount of dislocations creates local disorientation that affects the contrast (yellow arrows). After analysis, these areas appeared as a large cluster (yellow arrows) that was much thicker than the true thickness relative to the apparent width of the dislocations (Fig. 3 (c)). This probably leads to a local overestimation of the density. As a result, for this ferrite grain, the density was measured to be $(5.6 \pm 1.0) \times 10^{13} \text{ m}^{-2}$, see Table 3.

Finally, an austenitic grain subjected to 10% strain is displayed in Fig. 3(e). This grain is highly disoriented, resulting in significant contrast variations in the grain (red arrows). Although the dislocations present in austenite are easier to image using ECCI than those in ferrite, austenite deforms before ferrite, such that the dislocation densities

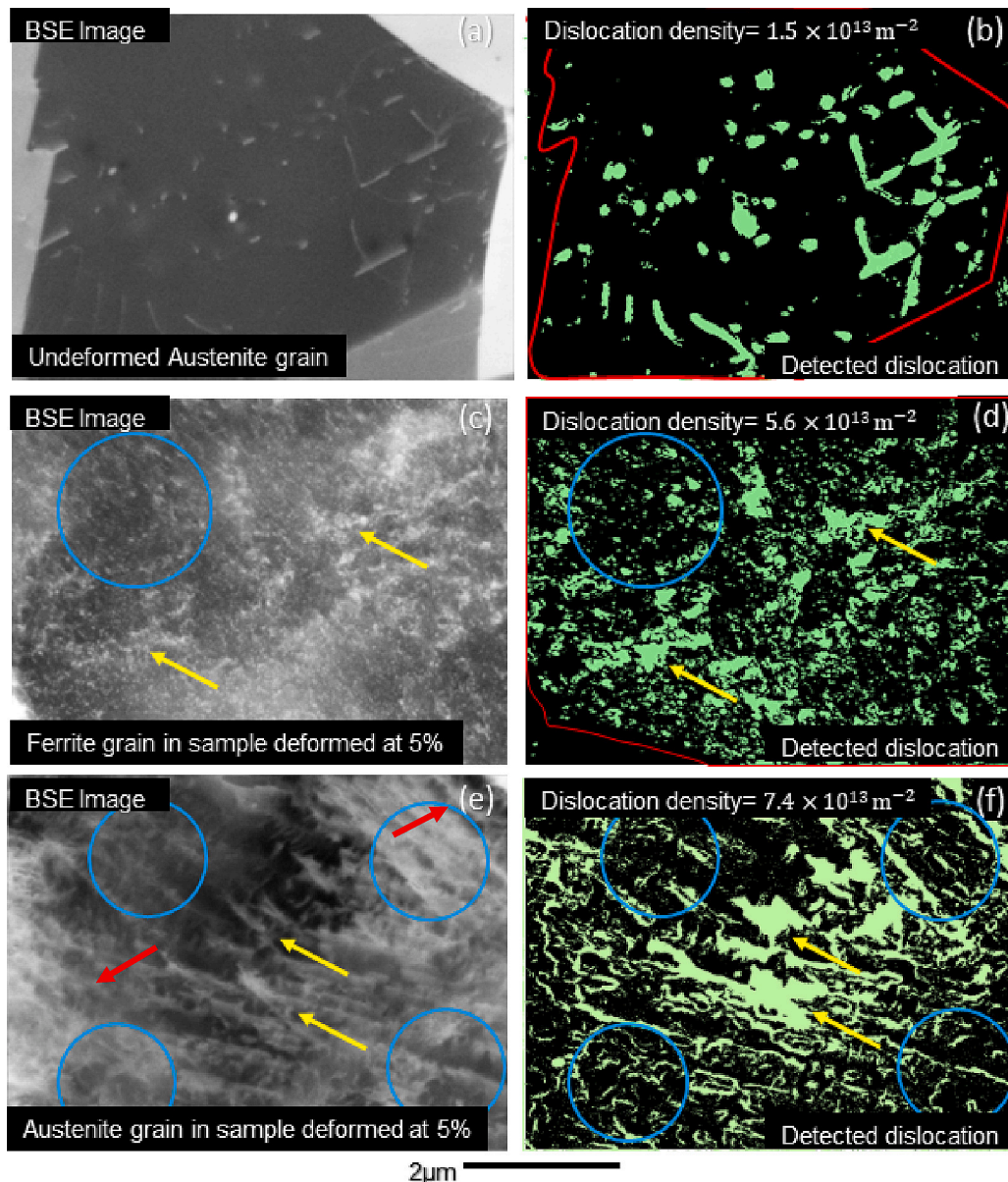


Fig. 3. BSE image acquired with an acceleration voltage of 20 keV, an aperture of 120 μm , and a pixel size of 4.5 nm. (a), (c), and (e) show an undeformed austenite grain (a), a ferrite grain present in a sample deformed at 5% (c), and an austenite grain present in a sample deformed at 10% (e). Images (b), (d), and (f) show the results obtained using the clustering algorithm, where the detected dislocations appear in green, and the densities thus measured on the grains (a), (c), and (e), respectively. Only the pixels in the red box in (b) and (d) were considered for the calculation of the dislocation densities. The blue circles highlight the areas where information was lost and all dislocations are not detected or only partially detected. The yellow arrows indicate the areas where dislocations are detected but much thicker than in the BSE images. (For interpretation of the references to colour in this figure legend, the reader is referred to the web version of this article.)

Table 3

: Mean value of the dislocation density (m^{-2}) obtained on ferrite and austenite grains for different strain rates measured from ECCI imaging.

	0%	5%	10%
Austenite	$(1.5 \pm 0.1) \times 10^{13}$	$(4.5 \pm 1.0) \times 10^{13}$	$(7.4 \pm 1.5) \times 10^{13}$
Ferrite	$(2.5 \pm 0.1) \times 10^{13}$	$(5.6 \pm 1) \times 10^{13}$	$(5.4 \pm 1) \times 10^{13}$

quickly reach values that are no longer measurable by clustering. Indeed, the dislocations form cells and become difficult to distinguish from each other. As with the previous ferritic grain, the clustering algorithm finds areas where all the dislocations are merged (yellow arrows in Fig. 3(f)), which results in an overestimation of the density. These “large clusters” partly stem from the strong contrast variation but also from the proximity or overlapping of the dislocations. Moreover, for certain areas, there is an information loss (blue circles). For this sample, the clustering is more efficient in the center of the image than on the edges because of the more important disorientation at the grain boundaries. For all these reasons, the obtained value of $(7.4 \pm 1.5) \times 10^{13} \text{ m}^{-2}$ seems underestimated. In that case, and for comparison's sake, single ECCI images were used and the dislocation densities were measured manually. The measured density for the 10% deformed austenite is $(1.3 \pm 0.4) \times 10^{14} \text{ m}^{-2}$, which confirms that this density is well beyond the current limits of the method.

4.3. Electron back scattered diffraction

Several EBSD acquisitions were performed for each strain rate. The areas selected generally covered both phases and contained interfaces or grain boundaries, where deformation is known to localize for this type of alloy. Note that the investigated areas were rather small ($5 \times 5 \mu\text{m}$ maximum). The acquisition time was limited to ~ 23 min per map, as the high sensitivity of the HR-EBSD technique can result in image drift becoming visible for longer acquisitions.

The orientation mappings were post-processed in a standard way by assessing the norm of the Nye tensor from the Euler angles. The so-obtained GND density maps are presented in Fig. 4, bottom row, and will be further discussed in light of the HR-EBSD measurements.

To obtain a dislocation density value that could be compared with that determined using the other used methods, average values were

Table 4

Average value of the dislocation density (m^{-2}) obtained with the norm of the Nye tensor in ferrite and austenite grains for different strain rates.

	0%	5%	10%
Austenite	$(1.2 \pm 0.7) \times 10^{14}$	$(2.1 \pm 0.8) \times 10^{14}$	$(3.3 \pm 1.2) \times 10^{14}$
Ferrite	$(4.6 \pm 1.4) \times 10^{13}$	$(1.1 \pm 0.5) \times 10^{14}$	$(2.1 \pm 0.9) \times 10^{13}$

calculated for each grain and are listed in Table 4. With increasing strain, the density in austenite (red in Fig. 4, top row) evolved faster than that contained in ferrite (blue), which is consistent with the known deformation of austenite before ferrite [62].

4.4. High resolution-electron back scattered diffraction

An HR-EBSD analysis was then conducted on each of the previous EBSD data sets. The strain concentration at the grain boundaries for both phases is more clearly observed from the GND mappings in Fig. 5.

As for EBSD, the dislocation density was averaged at the grain scale, and the values are summarized in Note that the largest discrepancy between EBSD and HR-EBSD is observed at 0% strain in austenite, where the value obtained by EBSD is twice as high as that obtained by HR-EBSD. Although this large gap is not observed in ferrite, it is not surprising that it is associated with the sample with the lowest grain internal disorientations. As previously mentioned, the uncertainty on the disorientation axis derived from Euler angles is maximal.

Table 5. Overall, both the EBSD and HR-EBSD techniques agree quite well; however, the average GND density obtained by EBSD is always higher than that obtained using HR-EBSD. This difference is attributed to the noisier character of the maps derived in Euler angles (Fig. 4), whereas the measurement uncertainty is estimated to be $1.1 \times 10^{13} \text{ m}^{-2}$ with HR-EBSD (minimum of GND obtained).

This noise is particularly visible in Fig. 4g, where the continuous red lines (indicated by black arrows) do not correspond to any obvious dislocation structure that the sensitivity of the HR-EBSD technique to orientation changes would have detected in Fig. 5g. This difference is also confirmed by the absence of such marked features in the virtual backscatter electron diode image in Fig. 6(a), although its contrast is very sensitive to orientation changes as well (see [34] for further details). Note that this approach only provides qualitative information,

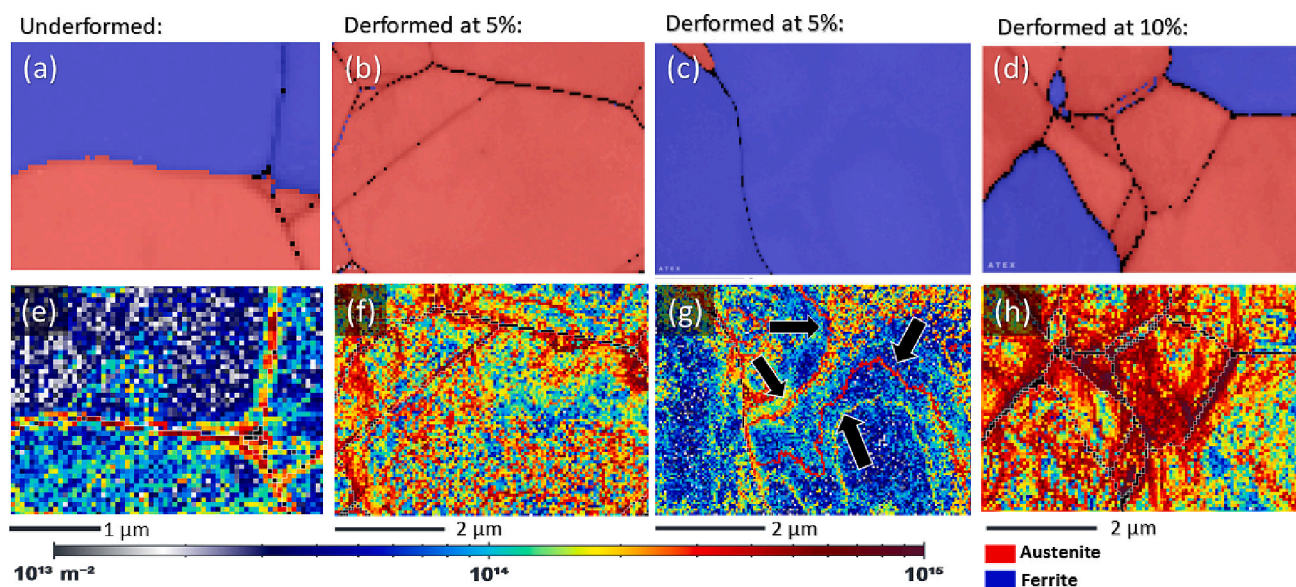


Fig. 4. Example of EBSD phase maps (top line, with austenite in red and ferrite in blue) obtained on undeformed, 5% deformed, and 10% deformed steel samples. Norm of Nye tensor map obtained by EBSD (bottom line). (For interpretation of the references to colour in this figure legend, the reader is referred to the web version of this article.)

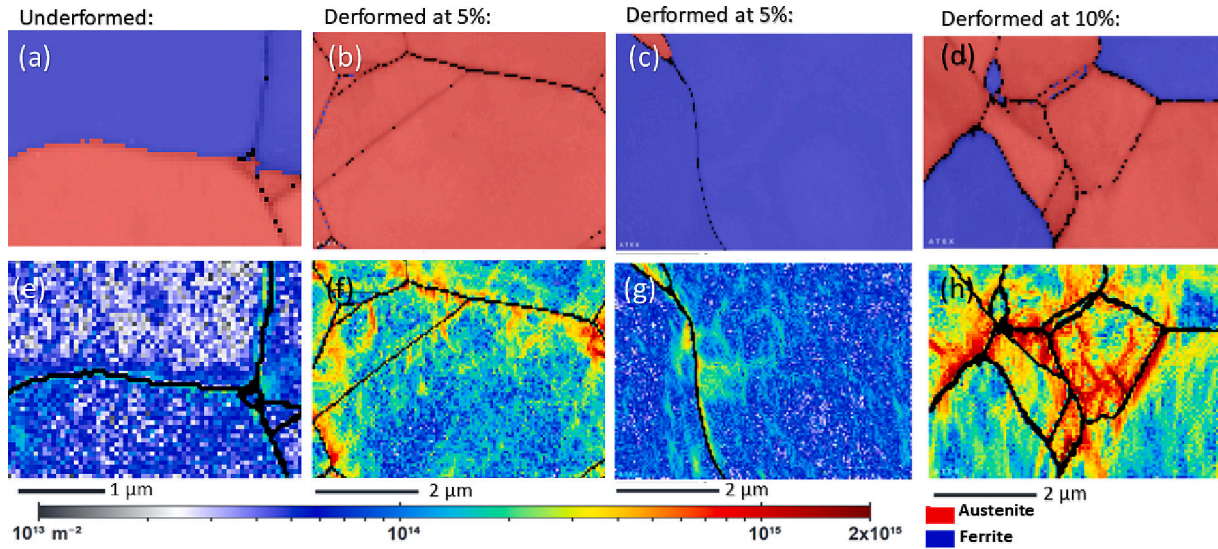


Fig. 5. Example of EBSD map (top line) obtained on undeformed, 5 and 10% deformed steel samples. GND-map obtained by HR-EBSD (bottom line).

Table 5

Average value of the dislocation density (m^{-2}) obtained using of HR-EBSD on ferrite and austenite grains for different strain rates.

	0%	5%	10%
Austenite	$(5.6 \pm 1.1) \times 10^{13}$	$(1.7 \pm 0.2) \times 10^{14}$	$(2.6 \pm 0.2) \times 10^{14}$
Ferrite	$(4.2 \pm 1.1) \times 10^{13}$	$(8.6 \pm 1.5) \times 10^{13}$	$(1.9 \pm 0.2) \times 10^{14}$

whereas the HR-EBSD technique is quantitative.

The aforementioned red lines in Fig. 4g originate from a discretization of orientations by the indexing software. Indeed, they superimpose with the relative rotation w_2 within the grain derived from Euler angles in Fig. 6(b), which locally presents discontinuities of the order of 0.2° , in agreement with the angular resolution of the indexing techniques. Note that the considered axis here is parallel to the image height; however, its use is not relevant for the purpose. The objective is to underline that knowledge of the disorientation axis is essential for the accurate assessment of GND densities (because a tensor is to be computed). For this reason, these artifacts are less visible from the disorientation angle in practice (not shown here), as the latter does not carry information about the axis.

Note that the largest discrepancy between EBSD and HR-EBSD is observed at 0% strain in austenite, where the value obtained by EBSD is twice as high as that obtained by HR-EBSD. Although this large gap is not observed in ferrite, it is not surprising that it is associated with the sample with the lowest grain internal disorientations. As previously mentioned, the uncertainty on the disorientation axis derived from Euler angles is maximal.

Overall, the average GND density obtained by HR-EBSD follows the same trends as that obtained using EBSD. Between the undeformed sample and the 5% deformed sample, the dislocation density in ferrite increases by a factor of 2, whereas in austenite, the evolution is 3 times faster. This slower increase in ferrite for the initial stages of the deformation is consistent with austenite deforming first. However, between the 5% deformed and 10% deformed stage, the dislocation density in the austenite continues increasing but at a slower rate than in the previous stage (from a factor of 3 to 1.5), whereas that in ferrite has a slightly higher increasing factor (increasing from 2 to 2.2).

4.5. X-ray diffraction

XRD patterns obtained for the 0%, 5%, and 10% deformed samples

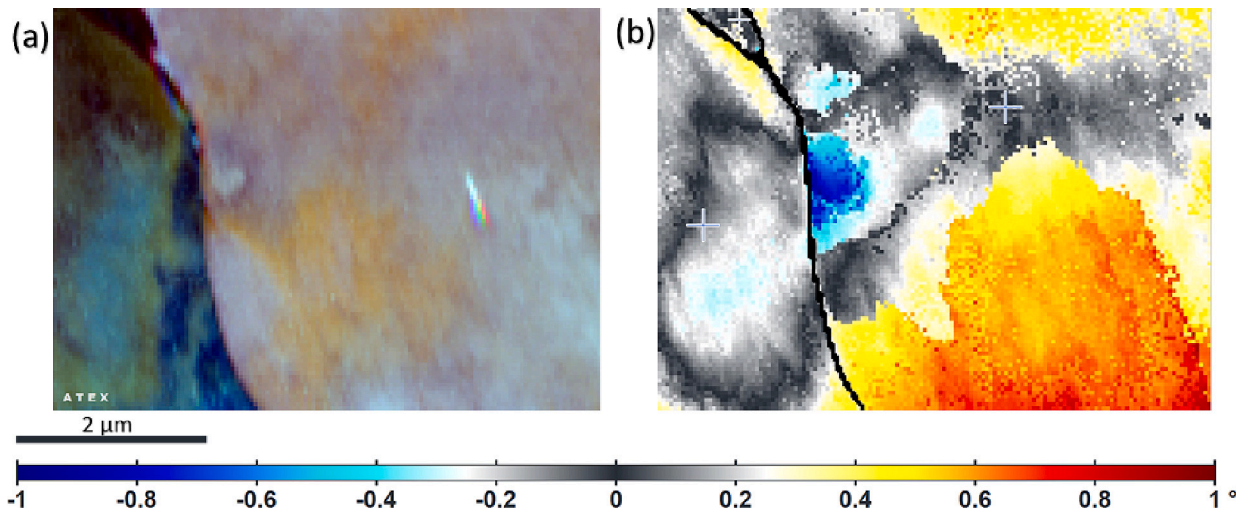


Fig. 6. (a) Virtual forescatter electron diode image computed from the Kikuchi patterns stored for the HR-EBSD analysis. (b) Relative rotation around the second axis of the sample frame. These rotations are computed from Euler angles relative to a reference point within each grain (indicated by the white cross).

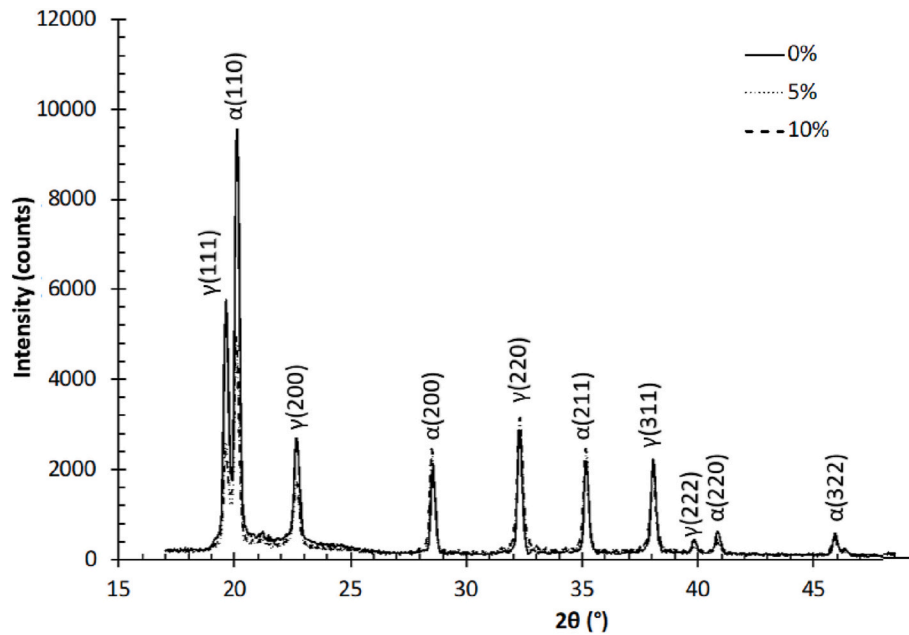


Fig. 7. Experimental XRD patterns for 0%, 5%, and 10% deformed samples.

Table 6

Average value of the dislocation density (m^{-2}) obtained using XRD on ferrite and austenite grains for different strain rates.

	0%	5%	10%
Austenite	$(4.0 \pm 10.7) \times 10^{13}$	$(1.7 \pm 0.3) \times 10^{14}$	$(1.8 \pm 0.3) \times 10^{14}$
Ferrite	$(6.1 \pm 13.1) \times 10^{13}$	$(7.6 \pm 4.6) \times 10^{13}$	$(9.0 \pm 2.6) \times 10^{13}$

are presented in Fig. 7.

The dislocation densities obtained for ferrite and austenite grains for different strain rates are summarized in Table 6.

The measurement uncertainties on the undeformed sample are on the order of 200%. This is because the RMS microstrain (ϵ_L^2) is included in the curve-fitting parameters and is difficult to obtain accurately on the undeformed sample. In the deformed sample, the RMS microstrain (ϵ_L^2) is higher and can be more precisely determined. Thus, its uncertainty drops by a factor of 10, and the global measurement uncertainty is then three to four times smaller.

During deformation, the dislocation density present in the austenite measured by XRD increases faster than that present in the ferrite, which is consistent with the deformation mechanism of a duplex steel [62]. For instance, the density in austenite is measured to be twice higher than that in ferrite after 5% and 10% deformation. After 10% deformation, the density does not evolve much compared with the 5% deformation case for both phases. For the austenite phase, the austenite grains were partly transformed into martensite. Thus, the crystallite size D was overestimated in this sample and the dislocation density present in the 10% deformed sample may be underestimated.

5. Discussion

All the methods presented here do not measure the same type of dislocation (ρ_c , ρ_w , ρ_{GB}). Moreover, each method has its own limitations and uncertainties, and it is thus important to compare them carefully.

Each measurement method relies on different computational means based on diffraction, disorientation, channeling contrast, or manual dislocation counting. Fig. 8(a) shows a schematic representation of the dislocation configuration that can be observed within one grain (group of random dislocations ρ_c , dislocation cell ρ_w , dislocations grouped at the grain boundary ρ_{GB}).

XRD measurements enable the measurement of disorientations within what is defined as crystallites, Fig. 8(b). This means that the dislocations close to the grain boundaries (ρ_{GB}) or grouped in cells (ρ_w), which are the main source of GNDs, will not be considered when calculating the dislocation density. Moreover, a crystallite is defined as an area showing a low disorientation; it can be a grain but also a dislocation cell. Therefore, dislocation cells will be seen as grains using this method. The size of the crystallite is often very complicated to determine [63] because it can vary enormously from case to case and it becomes difficult to calculate the size precisely if the shape of the crystallite [64] or the deformation [65] becomes anisotropic.

For TEM and ECCI imaging methods, dislocations are theoretically all visible; however, it is often very difficult to distinguish dislocations near grain boundaries as the disorientation is important and the conditions for observing dislocations change rapidly, Fig. 8(c). Moreover, imaging methods give images projected on a surface, and overlapping dislocations, such as at those present at grain boundaries or cell walls, cause a non-negligible uncertainty [52]. In practice, these methods were applied at the center of the grain (relatively far from ρ_{GB}) and cannot accurately measure the number of dislocations in cells or walls (ρ_w). For this reason, the densities measured by imaging can be considered to be mainly dislocations isolated from the dislocation clusters (ρ_c).

For the EBSD or HR-EBSD methods presented Fig. 8(d), the relative rotation and elastic strain fields are measured, and using these fields, a GND density is derived. The most influential parameter on the results is the pixel size used. As demonstrated by Jiang et al. [57], the dislocation density can vary by an order of magnitude when the pixel size is doubled. Indeed, if the maps are acquired with a very fine step, as in Fig. 8(d)(left), the dislocations will be discernible and will be defined as GNDs. However, if a larger step is used (as in Fig. 8(d)(right)), some dislocation clusters could have their Burgers vector opposed and no longer cause lattice rotation. These dislocations will then be considered as SSDs. As specified by Jiang et al. [57], these variations in the measured density are the consequence of a change in the threshold defined between SSDs and GNDs.

A quantitative comparison of all the measurements results is presented in Fig. 9. The values obtained for the 0% sample remain of the same order of magnitude regardless of the method, although the XRD measurement uncertainty is very high (270.9%, calculated using the method of Murugesan et al. [61]).

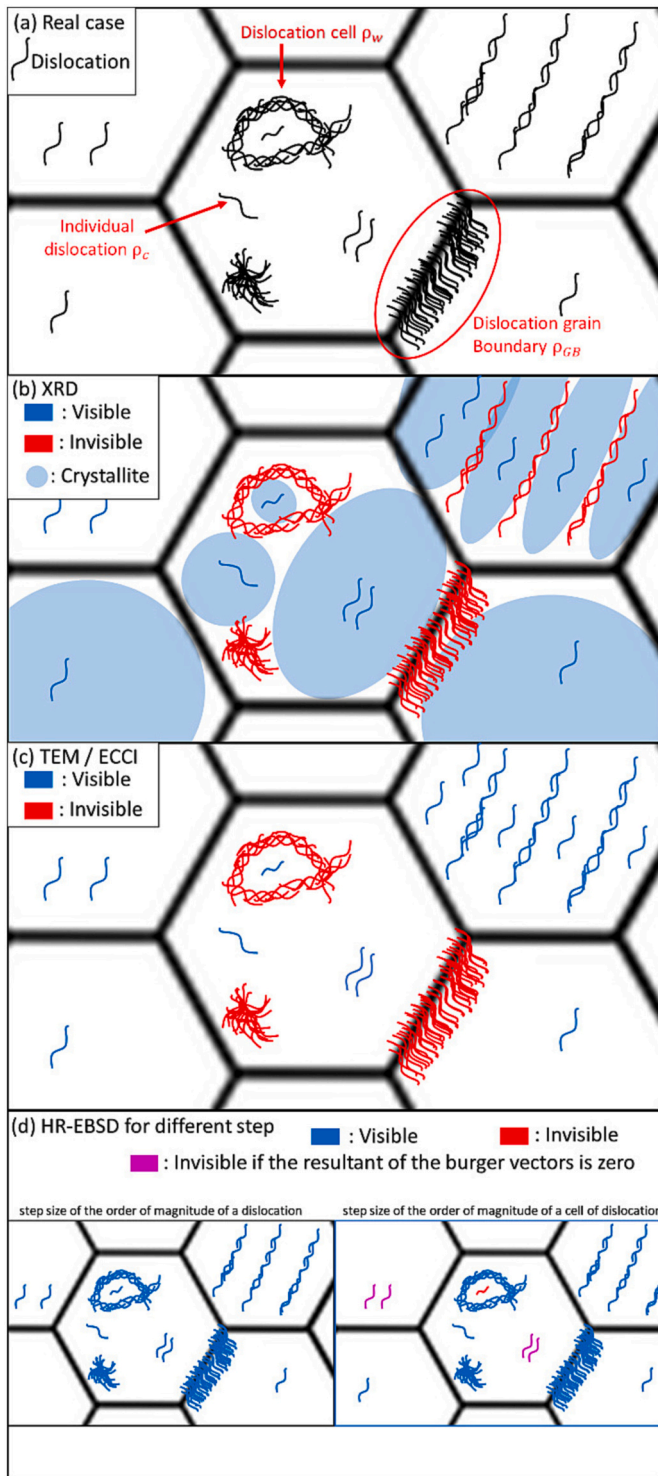


Fig. 8. Grain pattern with several cases of dislocations observable: dislocation cluster, isolated dislocation, dislocation cell, dislocation cluster present in particular planes. (a) Real case and (b) Illustration of dislocations analyzed by XRD and the crystallite size used. (c) Illustration of dislocations analyzed by TEM/ECCI imaging methods. (d) Two cases illustrating what the HR-EBSD method can distinguish depending on the pixel size used (very fine pixel size on the left and a larger pixel size on the right).

After 5% deformation, a higher dislocation density is expected in austenite compared to that in ferrite. The XRD and HR-EBSD results are similar to each other, and both indicate a dislocation density that is twice as high in austenite as in ferrite for this state (approximately $1.7 \times$

10^{14} m^{-2} and $0.7 \times 10^{14} \text{ m}^{-2}$, respectively). However, imaging-based measurements such as ECCI and TEM indicate smaller densities of approximately $5 \times 10^{13} \text{ m}^{-2}$ for both phases.

For the 10% deformed sample, ECCI measurements were not possible as the density was higher than the acceptable measurement range. All the other three methods reveal a large increase in the dislocation density. HR-EBSD gives the highest dislocation density with $(2.6 \pm 0.2) \times 10^{14} \text{ m}^{-2}$ for austenite and $(1.9 \pm 0.2) \times 10^{14} \text{ m}^{-2}$ for ferrite. In contrast, the TEM imaging results indicate a similar density for both phases with $(1.2 \pm 0.2) \times 10^{14} \text{ m}^{-2}$ for ferrite and $(1.4 \pm 0.3) \times 10^{14} \text{ m}^{-2}$ for austenite. Finally, the XRD measurements resulted in different densities for both phases with $(9.0 \pm 2.6) \times 10^{13} \text{ m}^{-2}$ for ferrite and $(1.8 \pm 0.3) \times 10^{14} \text{ m}^{-2}$ for austenite. These values are very close to those measured in the 5% deformed sample, which is quite surprising as the dislocation density was expected to increase between these two states.

We should note that the TEM, ECCI-based, and EBSD/HR-EBSD methods are all local measurement techniques that will provide data on a limited number of grains. In a polycrystalline material, the deformation process of individual grains is dependent on their relative orientation to the loading geometry and on their relative neighborhood. This is of particular importance in the present case as the steel is a bi-phased material. It is expected that the deformation process at interphases grain boundaries will be different than that at single phase grain boundaries.

5.1. SSD measurement (TEM; ECCI and XRD)

As explained before, we consider that ECCI and TEM observations provide mostly a determination of the SSD dislocation density. [66] Both methods are very local, therefore, one can expect similar measurements from both techniques. It is the case, considering the uncertainty of both measurements. However, we observed that for higher dislocation densities, and specifically for the 10% deformed sample, the disorientation within the grains and the dislocation overlapping made ECCI measurement irrelevant while some values could still be obtained from TEM measurements. We speculate that for those high-density values, it could be possible with TEM to obtain images close to the thin foil hole, i.e. in very thin areas, while the measurement depth is fixed for SEM-ECCI measurements and depends on the accelerating voltage selected. For ECCI measurements, the main uncertainty arises from the probed depth determination. The probed depth was assumed to be equal to $3\xi_g$ [54]; however, some authors have also reported values of $5\xi_g$ [67]. In the present case, the choice of $3\xi_g$ appeared to better reproduce the TEM observations.

The XRD measurements indicate an almost similar dislocation density for austenite and ferrite deformed at 5% and 10%, which is not representative of the microstructure expected. Sidor et al. [68] also observed this saturation in XRD measurements in a cold-rolled aluminum alloy. The densities obtained between two rolling steps remained equal to $(1.2 \pm 0.2) \times 10^{14} \text{ m}^{-2}$. This effect was explained by the dynamic equilibrium between dislocation multiplication and annihilation, resulting in a saturation of the dislocation density. However, in the present case, all other measurements methods indicate an increase in dislocation density between 5% and 10% deformation. In addition, the transformation of austenite into martensite during deformation was not taken into account. 316 L steels are mainly composed of austenite, which transform into martensite during deformation, thus decreasing the size of the crystallites, as shown by Han et al. [69] and Gubicza et al. [70]. The formation of this third phase in the steel studied here would therefore reduce the crystallite size D of the observed phases, which would increase the value of the density ρ_D (in eq. (13) for the 10% deformed sample).

XRD measurements are global measurements and should allow for the determination of SSD densities, similar to TEM and ECCI. Indeed, Lee et al. [71] reproduced a torsionally deformed copper sample using a finite element method (FEM). These researchers were able to compare

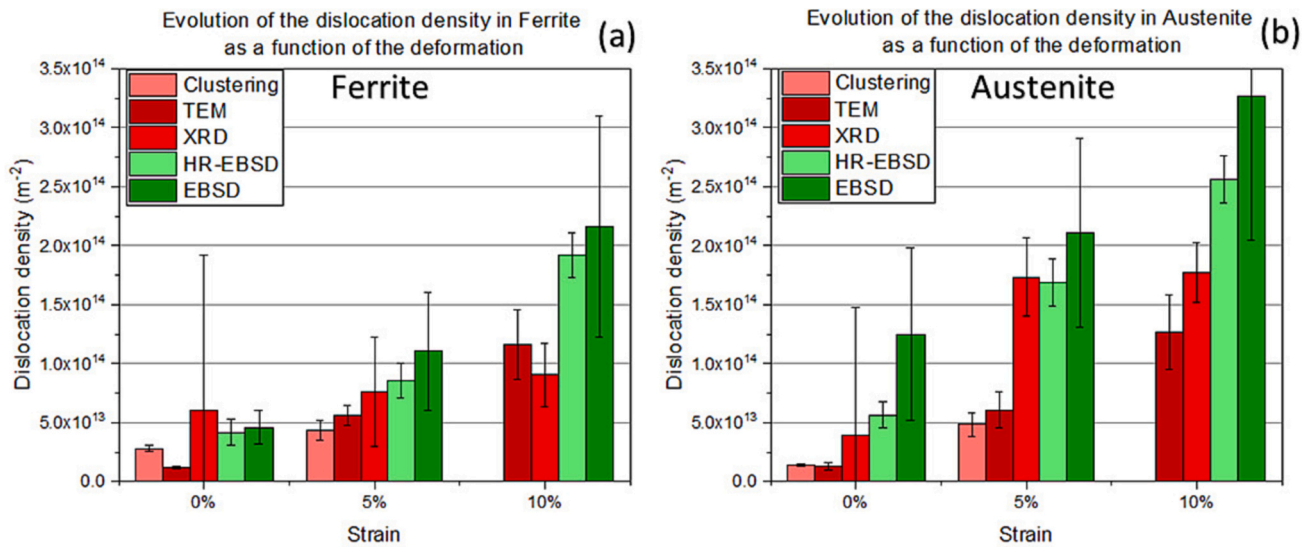


Fig. 9. Comparison of dislocation densities measured using XRD, TEM, HR-EBSD, and R-ECCI for (a) austenite and (b) ferrite in undeformed, 5% deformed, and 10% deformed samples.

their simulated value with the experimental TEM and XRD measurement, which allowed them to conclude that the dislocation density measured by XRD was located inside the cells, i.e. ρ_c . Even if the uncertainty in the measurement without deformation is very large for XRD measurements, the determined values are in the same range as those obtained by TEM/ECCI. The increase observed for 5% and 10% deformation in the ferrite is in fairly good agreement with the results obtained with the imaging techniques. However, for austenite, there is a much larger discrepancy between XRD and the imaging techniques. The obtained measurements are always slightly larger than those obtained using ECCI/TEM. A first reason for this difference could be the invisibility criterion, where only part of the dislocations can be visible at the same time from ECCI/TEM measurements. Moreover, TEM and ECCI measurements are subjected to surface effects. Surface dislocations are always subjected to the image force, which tends to attract them to the surface. There is a relaxation of the dislocation structure near the free surfaces of the sample, which extends approximately 65 nm into the sample, as demonstrated by Field et al. [72]. For TEM, the measurements are performed on a thin foil with a thickness of approximately 146 ± 10 nm; therefore, the image force cannot be neglected, and the dislocation density is underestimated. For instance, Kohnert et al. [73] determined that the structure of a bcc steel loses 40% of the dislocations it contains once it is in the state of a thin foil.

5.2. GND measurement (HR EBSD and EBSD)

The HR-EBSD method enables the expected localization of the deformation at grain boundaries to be visualized for this microstructure, Fig. 5. This phenomenon, which is explained by the incompatibility of the deformation between the two phases, is often observed in duplex steels [74] but also in dual phase steels [75].

Taking the average GND density for these maps appears to be biased as the disorientation is mainly located at the grain boundaries and there are very few grains present in totality in the maps. Moreover, as the results obtained using the two methods appear to converge for large deformations, the significant data storage (approximately 15 GB per map) and post-processing required by the HR-EBSD technique is no longer justified, and standard EBSD may be preferred. This result is observed because the uncertainty of indexing on the disorientation axis becomes less critical as the angular disorientation increases. For this reason, HR-EBSD measurements should be preferred at small deformation, where the contribution of elastic strains are not negligible and for

which the lower sensitivity of an indexing-based approach will prevent fine dislocation structures from being observed and quantified. In severely deformed materials, the degradation of the diffraction contrast in Kikuchi patterns strongly degrades the accuracy of HR-EBSD measurements. The slower acquisition speed and significant data storage associated with this technique is therefore no longer justified. In between these two extremes, a synergy of EBSD and HR-EBSD is expected. The former provides statistics while the latter can be applied to further investigate local details of the microstructure.

Finally, one must be cautious in the interpretation of GND mappings, especially when derived from Euler angles (EBSD). As pointed out in Fig. 4 and Fig. 6, GND mappings are sensitive to orientation noise and may present alleged dislocation walls, whereas they are artifacts. The latter typically result from a discretization of orientations, which occurs when using dictionary indexing techniques [76] or applying spatial filters (such as Kuhawara filters). Smoothing orientations to reduce noise in GND mappings is also not advisable, with GND accounting for discontinuities in the crystal orientations. Regarding HR-EBSD analyses, possible artifacts rather stem from drift during acquisition. Because of the higher sensitivity of the method, drift may become visible in the form of horizontal bands. The falsely associated GND density is, however, closer to the noise level than that observed in Fig. 4(f) with EBSD.

5.3. Discussion about the relative amount of GND and SSD

Although dislocation imaging by TEM or ECCI allows us to see both GND and SSD dislocations, mainly the measurement of ρ_c inside the grains, i.e. mainly SSD was performed in this study. An average of the XRD, TEM, and ECCI measurements is used to obtain a value of ρ_{SSD} , which is compared to the measurement obtained by HR-EBSD, ρ_{GND} . In Fig. 10, the ρ_{GND} and ρ_{SSD} densities are almost identical in the undeformed sample. During deformation, the GND densities increase faster than the SSD densities, especially for the 10% deformed sample. This result is consistent with the fact that the early stages of deformation are driven by austenite, as described by Zhang et al. [62]. However, the values obtained in the current study seem to contradict what is expected from the literature. Zheng et al. [77] observed from a high-energy XRD and TEM experiment in a pearlitic ferritic steel that the GND density is 10 times greater than the SSD density during deformation. In the 10% deformed sample, the GND density is only twice the SSD density. Furthermore, the factor of 2 measured for the 10% deformed sample appears to be inconsistent with the mechanical model results reported

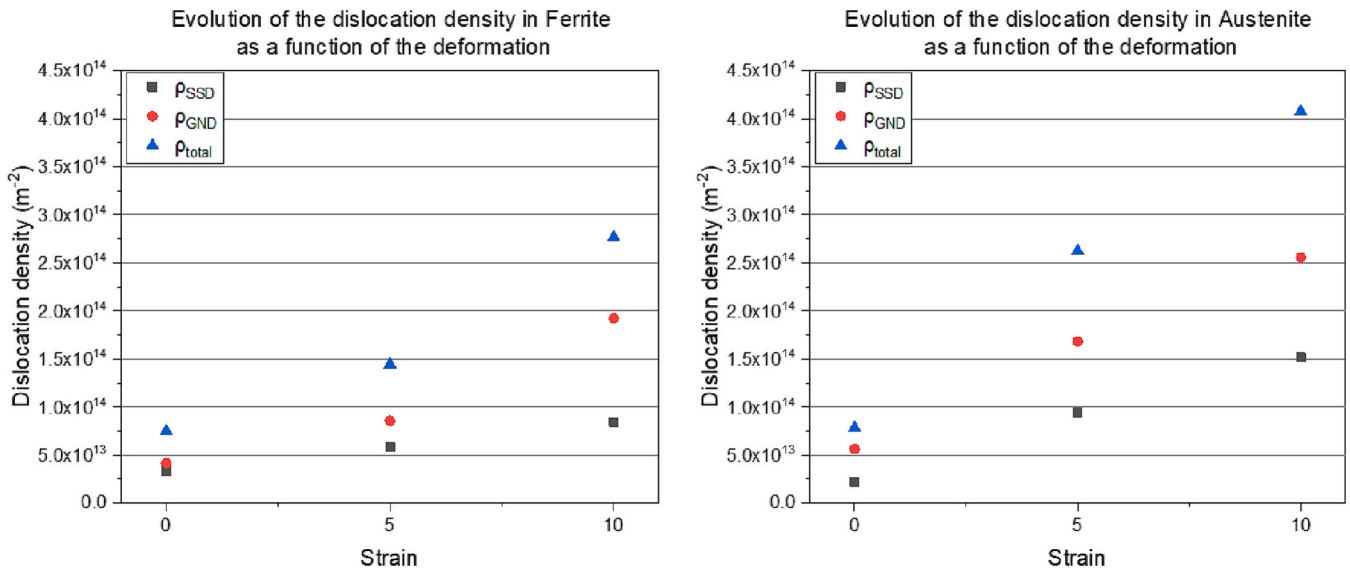


Fig. 10. Comparison of measured dislocation densities as a function of strain in (a) austenite and (b) ferrite in the undeformed, 5%, and 10% deformed samples. For ρ_{SSD} , the average of the measurements was obtained using XRD, TEM, and SEM imaging; for ρ_{GND} , the measurement was obtained using HR-EBSD; and ρ_{total} is the sum of ρ_{SSD} and ρ_{GND} .

by Zhi et al., namely the observation of approximately twice as many SSDs as GNDs during deformation in a TWIP steel [78].

As a conclusion, to better describe the full dislocation population (SSDs and GNDs), the complementary use of a diffracting method and an imaging method seems the best solution. In practice, this can be done using ECCI and EBSD / HR-EBSD on the same location, and with the same sample preparation, in the SEM. This would allow the measurement of ρ_c on one side and of ρ_w and ρ_{GB} on the other side.

5.4. Towards the prediction of yield stress

In multicomponent systems, the stress – strain curves can be modelled using mixture laws that describes the plastic strains of each phase. Bouquerel et al. [46] proposed an approximation that allows the description of the flow stress of each phase σ_y , considering solid solution strengthening (σ_i), grain boundary strengthening ($H_i/\sqrt{d_i}$) and dislocation strengthening σ_R . [44]:

$$\sigma_y = \sigma_i + H_i / \sqrt{d_i} + \alpha_i M_i \mu_i b_i \sqrt{\rho_i} \quad (15)$$

where $\sigma_R = \alpha_i M_i \mu_i b_i \sqrt{\rho_i}$ where α_i is the forest hardening coefficient of each phase i , M_i is the Taylor factor, μ_i is the elastic shear modulus, and b_i is the Burgers vector (for ferrite, it was considered that $b_i = b_{111}$).

Calculations were done for the ferritic phase at 0% deformation, see Table 7. The model and the values of the constants used were taken from the study by Chen et al. [44] When using the different values of the dislocation density obtained by the different methods, the values of σ_R differ by 69 MPa between $\rho_{Clustering}$ and $\rho_{SSD+GND}$ (see Table

The contribution due to SSD dislocations (TEM, ECCI-clustering and

Table 7
isotropic hardening obtained from the values of the different types of initial densities measured in the ferrite.

	ρ_0 (m ⁻²)	σ_R (MPa)
$\rho_{Clustering}$	$(2.5 \pm 0.1) \times 10^{13}$	108 ± 3
ρ_{TEM}	$(1.2 \pm 0.1) \times 10^{13}$	70 ± 3
ρ_{XRD}	$(6.1 \pm 13.1) \times 10^{13}$	159 ± 124
$\rho_{HR-EBSD}$	$(4.2 \pm 1.1) \times 10^{13}$	132 ± 19
ρ_{EBSD}	$(4.6 \pm 1.4) \times 10^{13}$	138 ± 23
$\rho_{SSD+GND}$	7.5×10^{13}	177

XRD), [73] lead to an error of a factor two depending on the choice of the characterization technique. However, for the determination of the contribution of GNDs to the YS, it is relatively equivalent to use results obtained from HR-EBSD or EBSD measurements. Finally, the variation of the total value of σ_R considering both GND and SSD contribution will be of 55,1 MPa. This represents 11% of the value of σ_y for ferrite in this case.

The determination of both GNDs and SSDs dislocations density can be done by a combination of R-ECCI and EBSD measurements. This will afford the best compromise in terms of sample preparation and observation time with measurement accuracy. This is of particular interest for this type of multi component systems as the same areas can be characterized using both techniques, and the large size of the samples can allow to choose adequate locations to feed the models (inside grains, at grains boundaries, at phase boundaries, etc....).

6. Conclusion

In this study, several approaches for measuring the dislocation density in deformed and undeformed materials were compared. XRD, EBSD, HR-EBSD, TEM, and ECCI imaging were used to determine the dislocation density present in industrial steel samples composed of austenite and ferrite phases for strain rates of 0%, 5%, and 10%.

The imaging methods saturate for densities above 10^{14} m⁻². The density obtained by XRD is always high and not very accurate for low densities. The HR-EBSD and classical EBSD methods appear to be more versatile for all the observed densities, and the increase of the dislocation density with the strain is well captured by EBSD and HR-EBSD. At the grain scale, the GND density obtained using both methods is very similar. Locally, the dislocation structures and strain concentration are better captured using the HR-EBSD technique.

Imaging techniques such as TEM and ECCI, as well as XRD, gave mostly information about the SSDs.

EBSD and HR-EBSD mainly measure the GND density. In this case, the EBSD and HR-EBSD measurements (GNDs) are always higher than the TEM, ECCI and XRD measurements (SSDs), and they are located at the grain boundaries.

The ratio between SSD and GND varies with the level of deformation; for the highest deformation cases, there are twice as many GNDs as SSDs. These differences directly affect the calculation of hardening in micro-mechanical models and must be carefully selected.

The combination of ECC imaging together with EBSD measurements can provide a full description of the dislocation population, and will provide a relatively good accuracy from low to quite large densities (10^{13} – 10^{15} m⁻²). Moreover, it can be performed on the same location, and with the same sample preparation, which signifies an important time saving compared to other measurements.

Declaration of Competing Interest

The authors declare that they have no known competing financial interests or personal relationships that could have appeared to influence the work reported in this paper.

Data availability

Data will be made available on request.

Acknowledgements

This work was conducted as part of the DISCO (Dislocation Imaging in Scanning electron microSCopy) project supported by the Institut Carnot Ingénierie@Lyon. The authors acknowledge Nicholas Blanchard for access to the TEM JEOL 2010 of the Centre Lyonnais de Microscopy (<http://www.clym.fr>).

References

- [1] J. Blaizot, T. Chaise, D. Nélis, M. Perez, S. Cazottes, P. Chaudet, Constitutive model for nickel alloy 690 (Inconel 690) at various strain rates and temperatures, *Int. J. Plast.* 80 (2016) 139–153.
- [2] G. Krauss, Deformation and fracture in martensitic carbon steels tempered at low temperatures, *Metall. Mater. Trans. B Process Metall. Mater. Process. Sci.* 32 (2001) 205–221.
- [3] M. Saeglitz, G. Krauss, Deformation, fracture, and mechanical properties of low-temperature-tempered martensite in SAE 43xx steels, *Metall. Mater. Trans. A* 28 (1997) 377–387.
- [4] C. Singh, A. Basu, G. Thomas, Quality of coal in integrated iron and steel plants in India with reference to available raw materials, *J. Inst. Eng. India Min. Met. Div. India* 58 (1978).
- [5] H. Mecking, U.F. Kocks, Kinetics of flow and strain-hardening, *Acta Metall.* 29 (1981) 1865–1875.
- [6] U.F. Kocks, H. Mecking, Physics and phenomenology of strain hardening: the FCC case, *Prog. Mater. Sci.* 48 (2003) 171–273.
- [7] Y. Estrin, H. Mecking, A unified phenomenological description of work hardening and creep based on one-parameter models, *Acta Metall.* 32 (1984) 57–70.
- [8] Y. Estrin, Constitutive modelling of creep of metallic materials: some simple recipes, *Mater. Sci. Eng. A* 463 (2007) 171–176.
- [9] J. Blaizot, Etude de l'influence des procédés de fabrication sur les propriétés mécaniques des alliages de nickel, Université de Lyon, 2016.
- [10] P. Diano, A. Muggeo, J.C. Van Duysen, M. Guttman, Relationship between microstructure and mechanical properties of alloy 690 tubes for steam generators, *J. Nucl. Mater.* 168 (1989) 290–294.
- [11] A. Borbély, J.H. Driver, T. Ungár, An X-ray method for the determination of stored energies in texture components of deformed metals; application to cold worked ultra high purity iron, *Acta Mater.* 48 (2000) 2005–2016, [https://doi.org/10.1016/S1359-6454\(99\)00457-7](https://doi.org/10.1016/S1359-6454(99)00457-7).
- [12] A. Wauthier-Monnin, T. Chauveau, O. Castelnau, H. Réglé, B. Bacroix, The evolution with strain of the stored energy in different texture components of cold-rolled IF steel revealed by high resolution X-ray diffraction, *Mater. Charact.* 104 (2015) 31–41, <https://doi.org/10.1016/j.matchar.2015.04.005>.
- [13] J.F. Nye, Some geometrical relations in dislocated crystals, *Acta Metall.* 1 (1953) 153–162, [https://doi.org/10.1016/0001-6160\(53\)90054-6](https://doi.org/10.1016/0001-6160(53)90054-6).
- [14] A.H. Cottrell, *The Mechanical Properties of Matter*, 1964.
- [15] M.F. Ashby, The deformation of plastically non-homogeneous materials, *Philos. Mag. J. Theor. Exp. Appl. Phys.* 21 (1970) 399–424.
- [16] S. Biroscu, G. Liu, R. Ding, J. Jiang, T. Simm, C. Deen, M. Whittaker, The dislocation behaviour and GND development in a nickel based superalloy during creep, *Int. J. Plast.* 118 (2019) 252–268.
- [17] J. Zhang, B. Wang, H. Wang, Geometrically necessary dislocations distribution in face-centred cubic alloy with varied grain size, *Mater. Charact.* 162 (2020), 110205.
- [18] D.A. Hughes, N. Hansen, D.J. Bammann, Geometrically necessary boundaries, incidental dislocation boundaries and geometrically necessary dislocations, *Scr. Mater.* 48 (2003) 147–153.
- [19] D.G. Brandon, Y. Komem, Quantitative analysis of dislocation distributions, *Metallography* 3 (1970) 111–126, [https://doi.org/10.1016/0026-0800\(70\)90010-8](https://doi.org/10.1016/0026-0800(70)90010-8).
- [20] D.B. Williams, C.B. Carter, *Transmission electron Microscopy: A Textbook for Materials Science*, 2nd ed, Springer, New York, 2008.
- [21] G. L'hôte, C. Lafond, P. Steyer, S. Deschanel, T. Douillard, C. Langlois, S. Cazottes, Rotational-Electron channeling contrast imaging analysis of dislocation structure in fatigued copper single crystal, *Scr. Mater.* 162 (2019) 103–107, <https://doi.org/10.1016/j.scriptamat.2018.10.050>.
- [22] S. Cazottes, A. Bechis, C. Lafond, G. L'hôte, C. Roth, T. Dreyfus, P. Steyer, T. Douillard, C. Langlois, Toward an automated tool for dislocation density characterization in a scanning electron microscope, *Mater. Charact.* 158 (2019), 109954, <https://doi.org/10.1016/j.matchar.2019.109954>.
- [23] W. Pantleon, Resolving the geometrically necessary dislocation content by conventional electron backscattering diffraction, *Scr. Mater.* 58 (2008) 994–997, <https://doi.org/10.1016/j.scriptamat.2008.01.050>.
- [24] B.S. El-Dasher, B.L. Adams, A.D. Rollett, Viewpoint: experimental recovery of geometrically necessary dislocation density in polycrystals, *Scr. Mater.* 48 (2003) 141–145, [https://doi.org/10.1016/S1359-6462\(02\)00340-8](https://doi.org/10.1016/S1359-6462(02)00340-8).
- [25] S. Sun, B.L. Adams, W.E. King, Observations of lattice curvature near the interface of a deformed aluminium bicrystal, *Philos. Mag. A* 80 (2000) 9–25, <https://doi.org/10.1080/01418610008212038>.
- [26] D.J. Prior, Problems in determining the misorientation axes, for small angular misorientations, using electron backscatter diffraction in the SEM, *J. Microsc.* 195 (1999) 217–225.
- [27] J. Wheeler, E. Mariani, S. Piazolo, D.J. Prior, P. Trimby, M.R. Drury, The weighted burgers vector: a new quantity for constraining dislocation densities and types using electron backscatter diffraction on 2D sections through crystalline materials, *J. Microsc.* 233 (2009) 482–494, <https://doi.org/10.1111/j.1365-2818.2009.03136.x>.
- [28] A.J. Wilkinson, D. Randman, Determination of elastic strain fields and geometrically necessary dislocation distributions near nanoindenters using electron back scatter diffraction, *Philos. Mag.* 90 (2010) 1159–1177, <https://doi.org/10.1080/14786430903304145>.
- [29] C. Ernould, B. Beausir, J.-J. Fundenberger, V. Taupin, E. Bouzy, Chapter five - applications of the method, in: M. Hÿtch, P.W. Hawkes (Eds.), *Adv. Imaging Electron Phys.*, Elsevier, 2022, pp. 155–215, <https://doi.org/10.1016/bs.aiep.2022.07.005>.
- [30] A.J. Wilkinson, G. Meaden, D.J. Dingley, High-resolution elastic strain measurement from electron backscatter diffraction patterns: new levels of sensitivity, *Ultramicroscopy* 106 (2006) 307–313, <https://doi.org/10.1016/j.ultramicro.2005.10.001>.
- [31] T. Vermeij, J.P.M. Hoefnagels, A consistent full-field integrated DIC framework for HR-EBSD, *Ultramicroscopy* 191 (2018) 44–50, <https://doi.org/10.1016/j.ultramicro.2018.05.001>.
- [32] T.J. Ruggles, G.F. Bomarito, R.L. Qiu, J.D. Hochhalter, New levels of high angular resolution EBSD performance via inverse compositional Gauss–Newton based digital image correlation, *Ultramicroscopy* 195 (2018) 85–92, <https://doi.org/10.1016/j.ultramicro.2018.08.020>.
- [33] Q. Shi, S. Roux, F. Latourte, F. Hild, Estimation of elastic strain by integrated image correlation on electron diffraction patterns, *Ultramicroscopy* 199 (2019) 16–33, <https://doi.org/10.1016/j.ultramicro.2019.02.001>.
- [34] C. Ernould, B. Beausir, J.-J. Fundenberger, V. Taupin, E. Bouzy, Global DIC approach guided by a cross-correlation based initial guess for HR-EBSD and on-axis HR-TKD, *Acta Mater.* 191 (2020) 131–148, <https://doi.org/10.1016/j.actamat.2020.03.026>.
- [35] C. Ernould, B. Beausir, J.-J. Fundenberger, V. Taupin, E. Bouzy, *Advances in Imaging and Electron Physics*, Volume 223, Edited by Martin Hÿtch, Peter W, Elsevier, Hawkes, 2022.
- [36] E. Kröner, *Kontinuumsstheorie der Versetzungen und Eigenspannungen*, Springer-Verlag, Berlin Heidelberg, 1958. <https://www.springer.com/de/book/9783540022619>.
- [37] S. Kalácska, Z. Dankházi, G. Zilahi, X. Maeder, J. Michler, P.D. Ispánovity, I. Groma, Investigation of geometrically necessary dislocation structures in compressed Cu micropillars by 3-dimensional HR-EBSD, *Mater. Sci. Eng. A* 770 (2020), 138499, <https://doi.org/10.1016/j.msea.2019.138499>.
- [38] S.S. Dhinwal, C. Ernould, B. Beausir, Facilitating the occurrence of dynamic recrystallization in plain extra low-carbon steel by warm asymmetric rolling, *Mater. Charact.* 189 (2022), 111942, <https://doi.org/10.1016/j.matchar.2022.111942>.
- [39] C. Ernould, B. Beausir, J.-J. Fundenberger, V. Taupin, E. Bouzy, Characterization at high spatial and angular resolutions of deformed nanostructures by on-axis HR-TKD, *Scr. Mater.* 185 (2020) 30–35, <https://doi.org/10.1016/j.scriptamat.2020.04.005>.
- [40] J. Jiang, T.B. Britton, A.J. Wilkinson, Evolution of dislocation density distributions in copper during tensile deformation, *Acta Mater.* 61 (2013) 7227–7239, <https://doi.org/10.1016/j.actamat.2013.08.027>.
- [41] T. Ungár, H. Mughrabi, D. Rönnpagel, M. Wilkens, X-ray line-broadening study of the dislocation cell structure in deformed [001]-orientated copper single crystals, *Acta Metall.* 32 (1984) 333–342, [https://doi.org/10.1016/0001-6160\(84\)90106-8](https://doi.org/10.1016/0001-6160(84)90106-8).
- [42] I. Gutierrez-Urrutia, D. Raabe, Dislocation density measurement by electron channeling contrast imaging in a scanning electron microscope, *Scr. Mater.* 66 (2012) 343–346, <https://doi.org/10.1016/j.scriptamat.2011.11.027>.
- [43] I. Gutierrez-Urrutia, S. Zaefferer, D. Raabe, Coupling of electron channeling with EBSD: toward the quantitative characterization of deformation structures in the SEM, *Jom* 65 (2013) 1229–1236.
- [44] L. Chen, Q. Jia, S. Hao, Y. Wang, C. Peng, X. Ma, Z. Zou, M. Jin, The effect of strain-induced martensite transformation on strain partitioning and damage evolution in

- a duplex stainless steel with metastable austenite, *Mater. Sci. Eng. A* 814 (2021), 141173.
- [45] A. Lechartier, N. Meyer, R. Estevez, M. Mantel, G. Martin, G. Parry, M. Veron, A. Deschamps, Deformation behavior of lean duplex stainless steels with strain induced martensitic transformation: role of deformation mechanisms, alloy chemistry and predeformation, *Materialia*. 5 (2019), 100190.
- [46] J. Bouquerel, K. Verbeken, B.C. De Cooman, Microstructure-based model for the static mechanical behaviour of multiphase steels, *Acta Mater.* 54 (2006) 1443–1456.
- [47] D.G. Brandon, Y. Komem, Quantitative analysis of dislocation distributions, *Metallography*. 3 (1970) 111–126.
- [48] D.B. Williams, C.B. Carter, *Transmission electron Microscopy: A Textbook for Materials Science*, 2nd ed, Springer, New York, 2008.
- [49] D.J.H. Cockayne, I.L.F. Ray, M.J. Whelan, Investigations of dislocation strain fields using weak beams, *Philos. Mag.* 20 (1969) 1265–1270.
- [50] P.B. Hirsch, F.J. Humphreys, The deformation of single crystals of copper and copper-zinc alloys containing alumina particles-I. macroscopic properties and workhardening theory, *Proc. R. Soc. Lond. Math. Phys. Sci.* 318 (1970) 45–72.
- [51] S. Cazottes, A. Bechis, C. Lafond, G. L'Hôte, C. Roth, T. Dreyfus, P. Steyer, T. Douillard, C. Langlois, Toward an automated tool for dislocation density characterization in a scanning electron microscope, *Mater. Charact.* 158 (2019), 109954, <https://doi.org/10.1016/j.matchar.2019.109954>.
- [52] J. Gallet, M. Perez, S. Dubail, T. Chaise, T. Douillard, C. Langlois, S. Cazottes, About the automatic measurement of the dislocation density obtained by R-ECCL, *Mater. Charact.* (2022), 112358, <https://doi.org/10.1016/j.matchar.2022.112358>.
- [53] C. Lafond, T. Douillard, S. Cazottes, P. Steyer, C. Langlois, Electron CHanneling ORientation determination (eCHORD): an original approach to crystalline orientation mapping, *Ultramicroscopy*. 186 (2017), <https://doi.org/10.1016/j.ultramic.2017.12.019>.
- [54] S. Zaefferer, N.-N. Elhami, Theory and application of electron channelling contrast imaging under controlled diffraction conditions, *Acta Mater.* 75 (2014) 20–50, <https://doi.org/10.1016/j.actamat.2014.04.018>.
- [55] B. Beausir, J.-J. Fundenberger, Analysis tools for electron and X-ray diffraction, ATEX - Software (2017). <http://www.atex-software.eu>.
- [56] C. Ernould, B. Beausir, J.-J. Fundenberger, V. Taupin, E. Bouzy, Integrated correction of optical distortions for global HR-EBSD techniques, *Ultramicroscopy*. 221 (2021), 113158, <https://doi.org/10.1016/j.ultramic.2020.113158>.
- [57] J. Jiang, T.B. Britton, A.J. Wilkinson, Measurement of geometrically necessary dislocation density with high resolution electron backscatter diffraction: effects of detector binning and step size, *Ultramicroscopy*. 125 (2013) 1–9.
- [58] C. Fressengeas, B. Beausir, C. Kerisit, A.-L. Helbert, T. Baudin, F. Brisset, M.-H. Mathon, R. Besnard, N. Bozzolo, On the evaluation of dislocation densities in pure tantalum from EBSD orientation data, *Mater. Technol.* 106 (2018) 604, <https://doi.org/10.1051/mattech/2018058>.
- [59] L. Lutterotti, Maud: a Rietveld analysis program designed for the internet and experiment integration, *Acta Crystallogr. A*. 56 (2000), s54.
- [60] S. Murugesan, P. Kuppusami, E. Mohandas, M. Vijayalakshmi, X-ray diffraction analysis of defects in cold worked type 316 stainless steel, in: *AIP Conf. Proc.*, American Institute of Physics, 2011, pp. 485–486.
- [61] S. Murugesan, P. Kuppusami, E. Mohandas, M. Vijayalakshmi, X-ray diffraction Rietveld analysis of cold worked austenitic stainless steel, *Mater. Lett.* 67 (2012) 173–176.
- [62] X. Zhang, P. Wang, D. Li, Y. Li, Multi-scale study on the heterogeneous deformation behavior in duplex stainless steel, *J. Mater. Sci. Technol.* 72 (2021) 180–188, <https://doi.org/10.1016/j.jmst.2020.09.023>.
- [63] T. Ungár, J. Gubicza, G. Ribárik, A. Borbély, Crystallite size distribution and dislocation structure determined by diffraction profile analysis: principles and practical application to cubic and hexagonal crystals, *J. Appl. Crystallogr.* 34 (2001) 298–310.
- [64] D. Louër, J.P. Auffrédic, J.I. Langford, D. Ciosmak, J.C. Niepce, A precise determination of the shape, size and distribution of size of crystallites in zinc oxide by X-ray line-broadening analysis, *J. Appl. Crystallogr.* 16 (1983) 183–191.
- [65] G. Caglioti, A.T. Paoletti, F.P. Ricci, Choice of collimators for a crystal spectrometer for neutron diffraction, *Nucl. Instrum.* 3 (1958) 223–228.
- [66] S.Y.P. Allain, O. Bouaziz, I. Pushkareva, C.P. Scott, Towards the microstructure design of DP steels: a generic size-sensitive mean-field mechanical model, *Mater. Sci. Eng. A* 637 (2015) 222–234.
- [67] A.J. Wilkinson, G.R. Anstis, J.T. Czernuszka, N.J. Long, P.B. Hirsch, Electron channelling contrast imaging of interfacial defects in strained silicon-germanium layers on silicon, *Philos. Mag. A*. 68 (1993) 59–80, <https://doi.org/10.1080/01418619308219357>.
- [68] J.J. Sidor, P. Chakravarty, J.G. Bátorfi, P. Nagy, Q. Xie, J. Gubicza, Assessment of dislocation density by various techniques in cold rolled 1050 aluminum alloy, *Metals*. 11 (2021) 1571.
- [69] J.-K. Han, X. Liu, I. Lee, Y.O. Kuzminova, S.A. Evlashin, K.-D. Liss, M. Kawasaki, Structural evolution during nanostructuring of additive manufactured 316L stainless steel by high-pressure torsion, *Mater. Lett.* 302 (2021), 130364.
- [70] J. Gubicza, M. El-Tahawy, Y. Huang, H. Choi, H. Choe, J.L. Lábár, T.G. Langdon, Microstructure, phase composition and hardness evolution in 316L stainless steel processed by high-pressure torsion, *Mater. Sci. Eng. A* 657 (2016) 215–223.
- [71] D.J. Lee, E.Y. Yoon, D.-H. Ahn, B.H. Park, H.W. Park, L.J. Park, Y. Estrin, H.S. Kim, Dislocation density-based finite element analysis of large strain deformation behavior of copper under high-pressure torsion, *Acta Mater.* 76 (2014) 281–293.
- [72] D.P. Field, K.R. Magid, I.N. Mastorakos, J.N. Florando, D.H. Lassila, J. W. Morris Jr., Mesoscale strain measurement in deformed crystals: a comparison of X-ray microdiffraction with electron backscatter diffraction, *Philos. Mag.* 90 (2010) 1451–1464.
- [73] A.A. Kohnert, H. Tummala, R.A. Lebensohn, C.N. Tomé, L. Capolungo, On the use of transmission electron microscopy to quantify dislocation densities in bulk metals, *Scr. Mater.* 178 (2020) 161–165.
- [74] H. Khatami-Hamedani, A. Zarei-Hanzaki, H.R. Abedi, A.S. Anoushe, L. P. Karjalainen, Dynamic restoration of the ferrite and austenite phases during hot compressive deformation of a lean duplex stainless steel, *Mater. Sci. Eng. A* 788 (2020), 139400.
- [75] A. Mathévon, Caractérisation et modélisation des évolutions microstructurales et des propriétés mécaniques durant le traitement thermique d'aciers Dual-Phase, 2020.
- [76] Y.-H. Chen, S.U. Park, D. Wei, G. Newstadt, M. Jackson, J.P. Simmons, M. De Graef, A.O. Hero, A dictionary approach to EBSD indexing, *ArXiv150207436 Phys. Stat.* (2015). <http://arxiv.org/abs/1502.07436> (accessed March 5, 2019).
- [77] C. Zheng, L. Li, Y. Wang, W. Yang, Z. Sun, Micromechanical behavior of eutectoid steel quantified by an analytical model calibrated by in situ synchrotron-based X-ray diffraction, *Mater. Sci. Eng. A* 631 (2015) 181–188, <https://doi.org/10.1016/j.msea.2015.02.003>.
- [78] H. Zhi, C. Zhang, S. Antonov, H. Yu, T. Guo, Y. Su, Investigations of dislocation-type evolution and strain hardening during mechanical twinning in Fe-22Mn-0.6C twinning-induced plasticity steel, *Acta Mater.* 195 (2020) 371–382, <https://doi.org/10.1016/j.actamat.2020.05.062>.